PHYSICAL REVIEW C **85**, 034612 (2012)

Isotopic trends of capture cross section and mean-square angular momentum of the captured system

R. A. Kuzyakin, V. V. Sargsyan, G. G. Adamian, and N. V. Antonenko
Joint Institute for Nuclear Research, 141980 Dubna, Russia

E. E. Saperstein
Kurchatov Institute, 123182 Moscow, Russia

S. V. Tolokonnikov
Kurchatov Institute, 123182 Moscow, Russia, and Moscow Institute of Physics and Technology, 123098 Moscow, Russia

(Received 7 December 2011; published 23 March 2012)

Within the quantum diffusion approach, the isotopic dependencies of capture cross section and mean-square angular momentum are studied in the reactions ^{4}He, ^{16}O, ^{36}S, ^{48}Ca + ^{196,200,204,208}Pb and ^{16}O + ^{70,72,74,76}Ge. The results are in a reasonable agreement with existing experimental data.

DOI: 10.1103/PhysRevC.85.034612 PACS number(s): 25.70.Jj, 24.10.−i, 24.60.−k

I. INTRODUCTION

Recently many experimental and theoretical studies have been devoted to investigation of fusion, fission, and capture processes at sub-barrier energies [1–11]. Measurements of excitation functions down to the extreme sub-barrier energies are important for studying the long-range behavior of the nucleus-nucleus interaction. The experimental data obtained are also of interest for solving astrophysical problems related to nuclear synthesis in stars. There are indications for an enhancement of the so-called S factor [12,13] at energies $E_{\mathrm{c.m.}}$ below the Coulomb barrier but its origin is still under discussion.

The main objective of the present work is to analyze isotopic dependency of the capture cross section and the mean-square angular momentum in the reactions ^{4}He, ^{16}O, ^{36}S, ^{48}Ca + ^{196,200,204,208}Pb by using the quantum diffusion approach [9–11,14,15]. In this approach, collisions of nuclei are treated in terms of a single collective variable, the relative distance between the colliding nuclei. For deformed nuclei, deformation effects are taken into consideration through the dependence of the nucleus-nucleus potential on the deformations and orientations of colliding nuclei. Our approach takes into consideration the fluctuation and dissipation effects in collisions of heavy ions that model the coupling with various channels. We have to mention that many quantum mechanical and non-Markovian effects accompanying the passage through the potential barrier are taken into consideration in our formalism [9,10]. It should be noted that the diffusion model which includes the quantum statistical effects was also proposed in Refs. [7,16,17].

The isotopic dependence of the capture cross section is caused by the following reasons. The deformations of colliding nuclei depend on the neutron number. The isotopic effects are attributed to the neutron transfer if the Q value promotes it. The nucleon distributions in the nuclei are the functions of the mass numbers and affect the nucleus-nucleus potential. In this article we treat the reactions with the isotopes of lead, which are spherical. Moreover, the neutron transfer channels are negligible in these reactions because of the negative Q values. Thus, the nucleus-nucleus interaction potential remains the important ingredient of our approach, which depends on the isotopic composition of colliding nuclei.

For finding the nuclear part of the nucleus-nucleus potential, we follow Refs. [9,10], where the double-folding procedure was carried out with a density-dependent effective NN interaction as suggested in Ref. [18]. This interaction is found with some averaging ansatz starting from the density-dependent effective interaction of the theory of finite Fermi systems (TFFS) [19]. For density distributions of interacting nuclei, the two-parameter symmetrized Fermi-type form is used. For the lead isotopes, the Fermi distribution parameters are fitted to the self-consistent density distributions found within the energy density functional (EDF) method of Ref. [20] with the DF3-a functional [21].

II. MODEL

A. Nucleus-nucleus interaction potential

In the model [9,10], the potential describing the interaction of two nuclei is taken in the form [18]

$$V(R,Z_i,A_i,\theta_i,J)=V_C(R,Z_i,A_i,\theta_i)+V_N(R,Z_i,A_i,\theta_i)\\+V_{rot}(R,A_i,J), \qquad (1)$$

where V_N, V_C, and the last summand stand for the nuclear, the Coulomb, and the centrifugal potentials, respectively. The nuclei are proposed to be spherical or deformed with the quadrupole deformation parameters β_i. The quadrupole deformation parameters are taken from Ref. [22] for even-even deformed nuclei. The nucleus-nucleus potential depends on the distance R between the center of mass (c.m.) of two interacting nuclei, their masses A_i and charges Z_i ($i=1,2$), the orientation angles θ_i for deformed nuclei, and the relative angular momentum J. The index $i=1$ marks the lighter participant of the collision process and $i=2$ marks the heavier one.

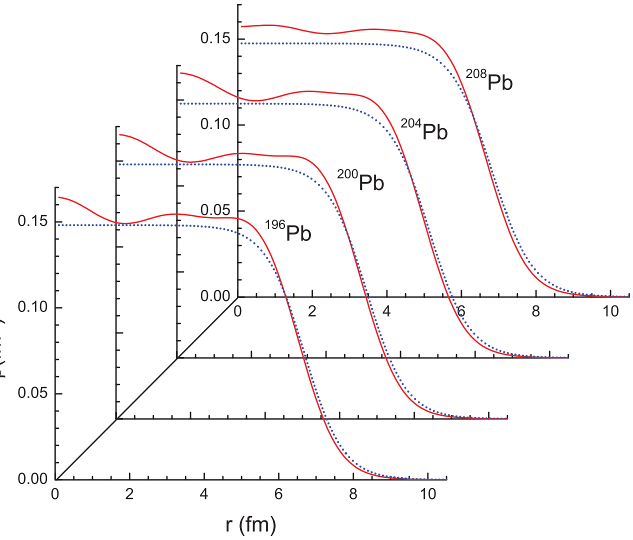

FIG. 1. (Color online) Comparison of the self-consistent density distributions (solid lines) with Fermi approximations (dotted lines) for four Pb isotopes.

For the nuclear part of the nucleus-nucleus potential, we use the double-folding formalism, in the form

$$V_N(R, Z_i, A_i, \theta_i) = \int \rho_1(\mathbf{r}_1)\rho_2(\mathbf{R}-\mathbf{r}_2)F(\mathbf{r}_1-\mathbf{r}_2)d\mathbf{r}_1 d\mathbf{r}_2, \tag{2}$$

with the density-dependent effective NN interaction

$$F(\mathbf{r}_1-\mathbf{r}_2) = C_0\left[F_{\text{in}}\frac{\rho(\mathbf{r}_1)}{\rho_0} + F_{\text{ex}}\left(1-\frac{\rho(\mathbf{r}_1)}{\rho_0}\right)\right]\delta(\mathbf{r}_1-\mathbf{r}_2). \tag{3}$$

Here $C_0 = 300$ MeV fm^3 is the usual TFFS normalization parameter and $\rho(\mathbf{r}) = \rho_1(\mathbf{r}) + \rho_2(\mathbf{R}-\mathbf{r})$ is the total nucleon density of the dinuclear system. The interaction strengths in Eq. (3) are found in terms of Landau-Migdal parameters f, f'

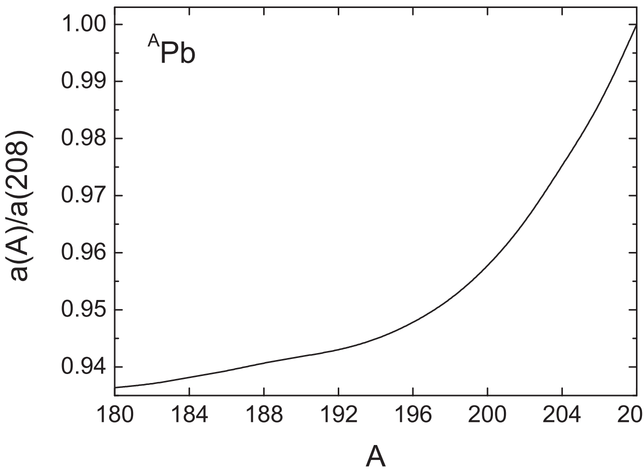

FIG. 2. Dependence of the diffuseness parameter a on the mass number A of even-even Pb isotopes. Calculations were performed within FFST in Ref. [23].

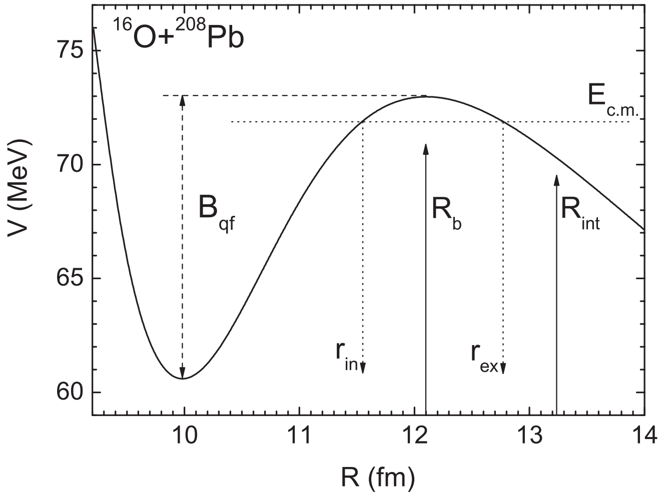

FIG. 3. The nucleus-nucleus interaction potential calculated for the ^{16}O + ^{208}Pb reaction at zero angular momentum. The position R_b of the Coulomb barrier, radius of interaction R_{int}, and the external r_{ex} and the internal r_{in} turning points for some values of $E_{\text{c.m.}}$ are indicated.

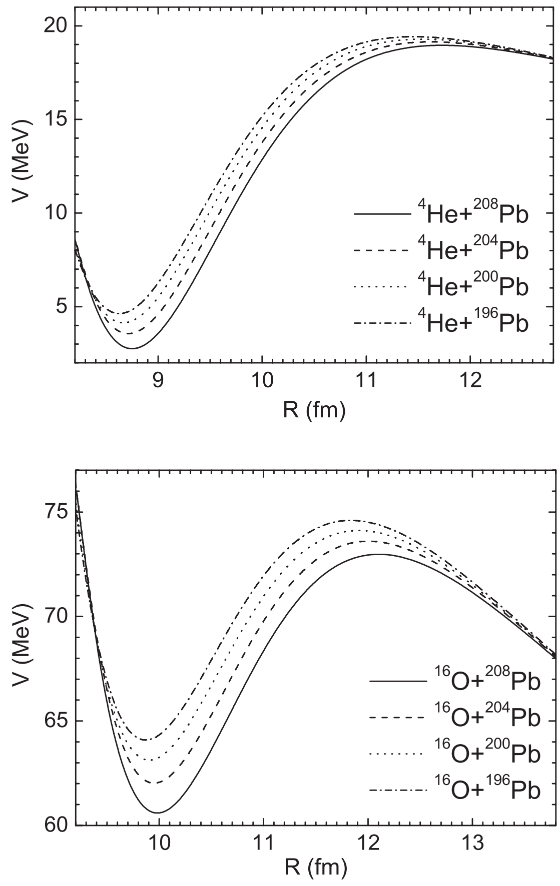

FIG. 4. The nucleus-nucleus potentials calculated for the reactions ^{4}He + ^{196,200,204,208}Pb (upper part) and ^{16}O + ^{196,200,204,208}Pb (lower part) at zero angular momentum.

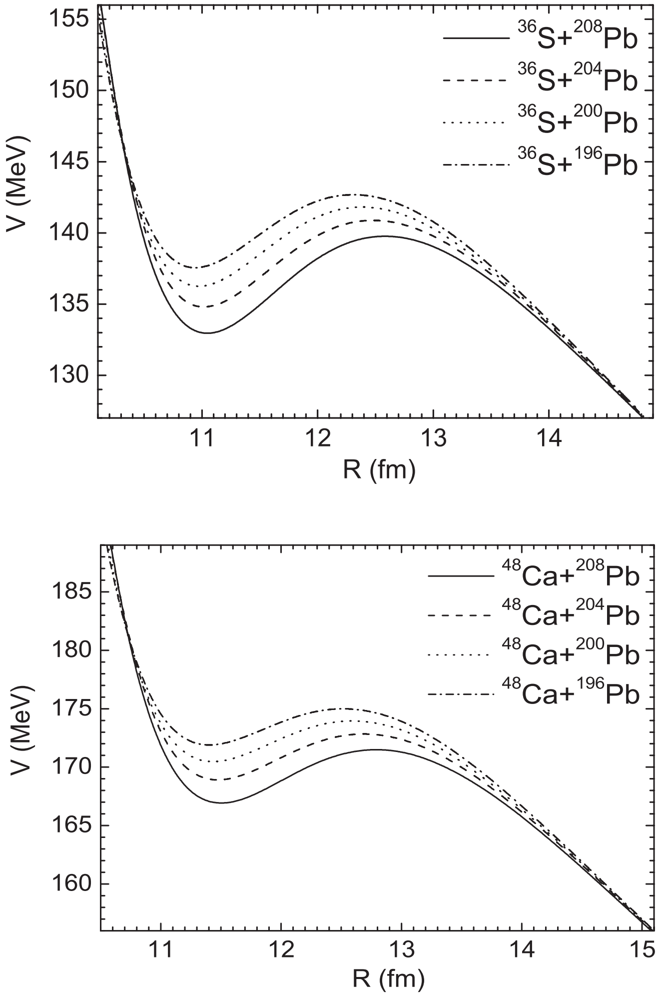

FIG. 5. The nucleus-nucleus potentials calculated for the reactions ^{36}S + ^{196,200,204,208}Pb (upper part) and ^{48}Ca + ^{196,200,204,208}Pb (lower part) at zero angular momentum.

with the averaging ansatz [18],

$$F_{\text{in,ex}} = f_{\text{in,ex}} + f'_{\text{in,ex}} \frac{(N_1 - Z_1)(N_2 - Z_2)}{(N_1 + Z_1)(N_2 + Z_2)}, \qquad (4)$$

where $N_i = A_i - Z_i$ are the neutron numbers of interacting nuclei. Our calculations are performed with the following set of parameters: $f_{\text{in}} = 0.09$, $f_{\text{ex}} = -2.59$, $f'_{\text{in}} = 0.42$, $f'_{\text{ex}} = 0.54$, and $\rho_0 = 0.17\ \text{fm}^{-3}$ [18]. To calculate the Coulomb and centrifugal potentials, we use the formulas

$$V_C(R, Z_i, A_i, \theta_i) = \frac{Z_1 Z_2 e^2}{A_1 A_2} \int \frac{\rho_1(\mathbf{r}_1)\rho_2(\mathbf{r}_2)}{|\mathbf{R} + \mathbf{r}_2 - \mathbf{r}_1|} d\mathbf{r}_1 d\mathbf{r}_2 \qquad (5)$$

and

$$V_{rot}(R, A_i, J) = \frac{\hbar^2 J(J+1)}{2\mu R^2}, \qquad (6)$$

where $P_2(\cos\theta_i)$ is the Legendre polynomial and $\mu = m A_1 A_2/(A_1 + A_2)$ is the reduced mass (m is the nucleon mass).

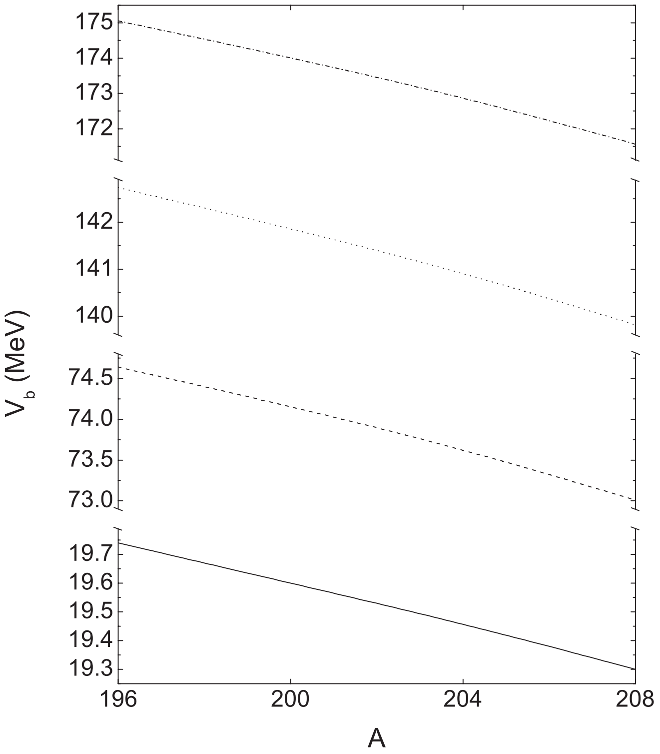

FIG. 6. The heights V_b of the Coulomb barriers calculated for the reactions ^{4}He + ^{A}Pb (solid line), ^{16}O + ^{A}Pb (dashed line), ^{36}S + ^{A}Pb (dotted line), and ^{48}Ca + ^{A}Pb (dash-dotted line) at zero angular momentum.

B. Nuclear density distributions

The density distributions ρ_1 and ρ_2 of interacting nuclei in Eqs. (2) and (3) are taken in the two-parameter symmetrized Fermi-type form with the nuclear radius parameter $r_0 = 1.15$ fm ($R = r_0 A_{1/3}$) for all nuclei with $A_i \geqslant 16$ and the diffuseness parameter a depending on the (A, Z) values of the nucleus under consideration [18]. Specifically, we use $a = 0.53$ fm for the light magic ^{16}O projectile and $a = 0.55$ fm for the intermediate-weight projectile nuclei ^{36}S, ^{48}Ca. For the lightest ^{4}He projectile the Fermi density parameters are taken equal to $r_0 = 1.02$ fm and $a = 0.48$ fm.

For nuclear density distributions of the long chain of lead isotopes, we start from the self-consistent density distributions found within the EDF method of Ref. [20] with the energy functional DF3-a [21]. It differs from the initial functional DF3 of Ref. [20] with spin-orbit and effective tensor components only. It made it possible to describe successfully the ground-state properties of nuclei from the calcium region to the transuranium one. In particular, the charge radii are reproduced with this functional with the record accuracy of $0.01 \div 0.02$ fm [23]. Then we approximate these density distributions with Fermi functions by fitting the parameters r_0 and a. It turned out that the regular value of $r_0 = 1.15$ fm is valid in this case, too. For the diffuseness parameters, we found $a = 0.520$, 0.526, 0.535, and 0.550 fm for four even lead isotopes ^{196}Pb, ^{200}Pb, ^{204}Pb, and ^{208}Pb, respectively. Quality of fitting is demonstrated in Fig. 1. It should be stressed that the "tails" of the density distributions mainly contribute to

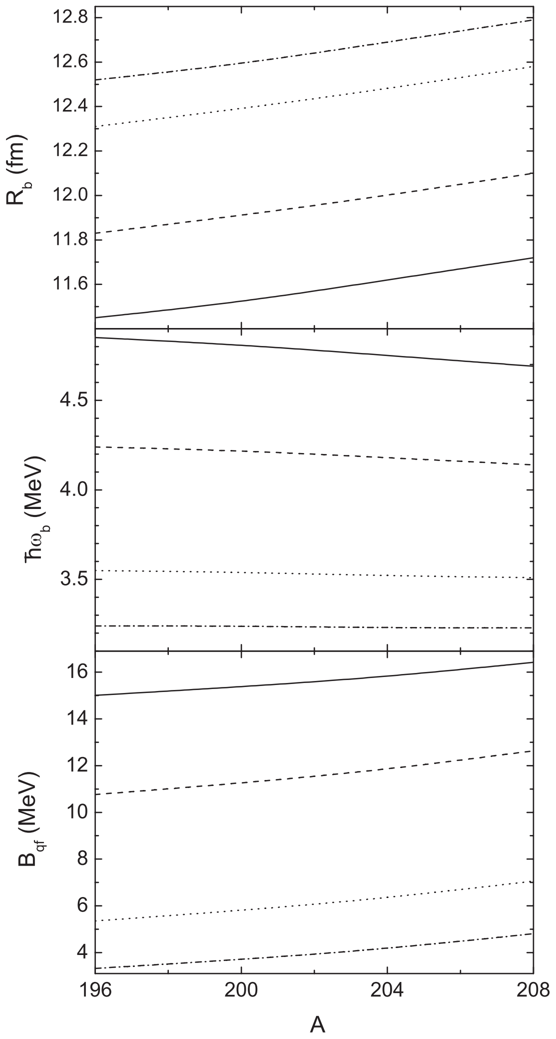

FIG. 7. The values of positions R_b of the Coulomb barriers (upper part), $\omega_b = |\partial^2 V/\partial R^2|_{R=R_b}$ (middle part), and B_{qf} (lower part) calculated for the reactions ^{4}He + ^{A}Pb (solid line), ^{16}O + ^{A}Pb (dashed line), ^{36}S + ^{A}Pb (dotted line), and ^{48}Ca + ^{A}Pb (dash-dotted line) at zero angular momentum.

the folding integral (2). Therefore, the differences between the self-consistent density distributions and the Fermi ones, which are seen in the central regions, are not important for the results. The values of the diffuseness parameter a for all lead isotopes are displayed in Fig. 2. One can see that the $a(A)$ dependence is, in general, essentially nonlinear and is characterized by a steep dropoff with A decreasing from 208 to 194 and by almost linear plot for values of A from 194 to 180.

C. Capture cross section and mean-square angular momentum of captured system

The capture cross section is a sum of partial capture cross sections $\sigma_{\rm cap}(E_{\rm c.m.}, J)$ [9,10]

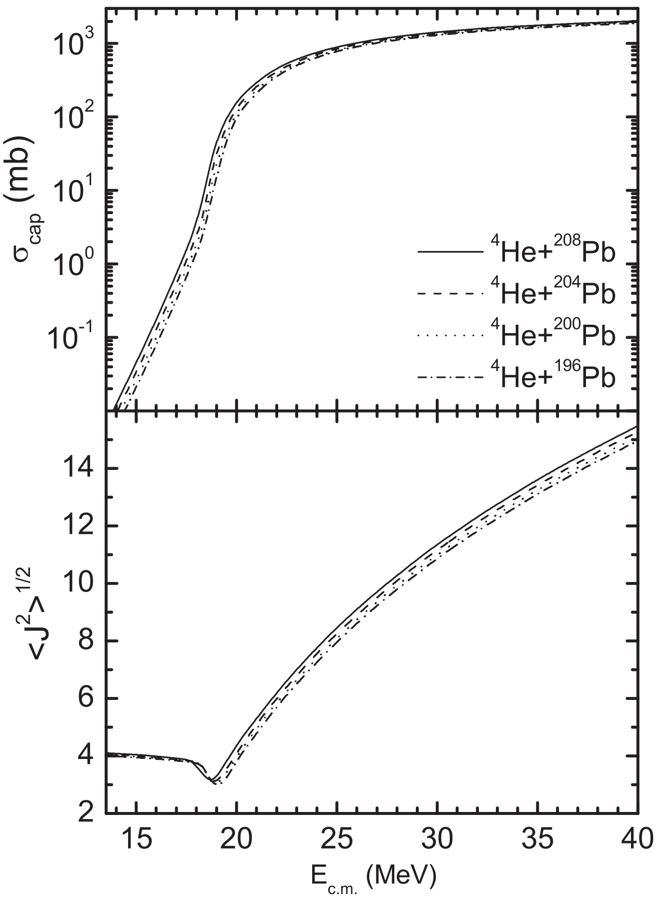

FIG. 8. The calculated capture cross sections (upper part) and the mean-square angular momenta of the captured system (lower part) vs $E_{\rm c.m.}$ for the reactions ^{4}He + ^{196,200,204,208}Pb. The heights V_b of the Coulomb barriers are 19.7 MeV, 19.6 MeV, 19.5 MeV, and 19.3 MeV, respectively.

$$\begin{aligned}\sigma_{\rm cap}(E_{\rm c.m.}) &= \sum_J \sigma_{\rm cap}(E_{\rm c.m.}, J)\\ &= \frac{\pi\hbar^2}{2\mu E_{\rm c.m.}} \sum_J (2J+1) \int_0^{\pi/2} d\theta_1 \sin\theta_1\\ &\quad\times \int_0^{\pi/2} d\theta_2 \sin\theta_2 P_{\rm cap}(E_{\rm c.m.}, J, \theta_1, \theta_2), \quad (7)\end{aligned}$$

where the summation is over the possible values of angular momentum J at a given bombarding energy $E_{\rm c.m.}$ in the center-of-mass system. Knowing the potential of the interacting nuclei for each orientation, one can obtain the partial capture probability $P_{\rm cap}$, which is defined by the passing probability of the potential barrier in the relative distance R at a given J. The mean-square angular momentum of captured system is calculated with the following formula:

$$\langle J^2 \rangle = \frac{1}{\sigma_{\rm cap}(E_{\rm c.m.})} \sum_J J(J+1)\sigma_{\rm cap}(E_{\rm c.m.}, J). \quad (8)$$

The value of $P_{\rm cap}$ is obtained by integrating the propagator G from the initial state (R_0, P_0) at time $t = 0$ to the final state (R, P) at time t (P is a momentum) [9]:

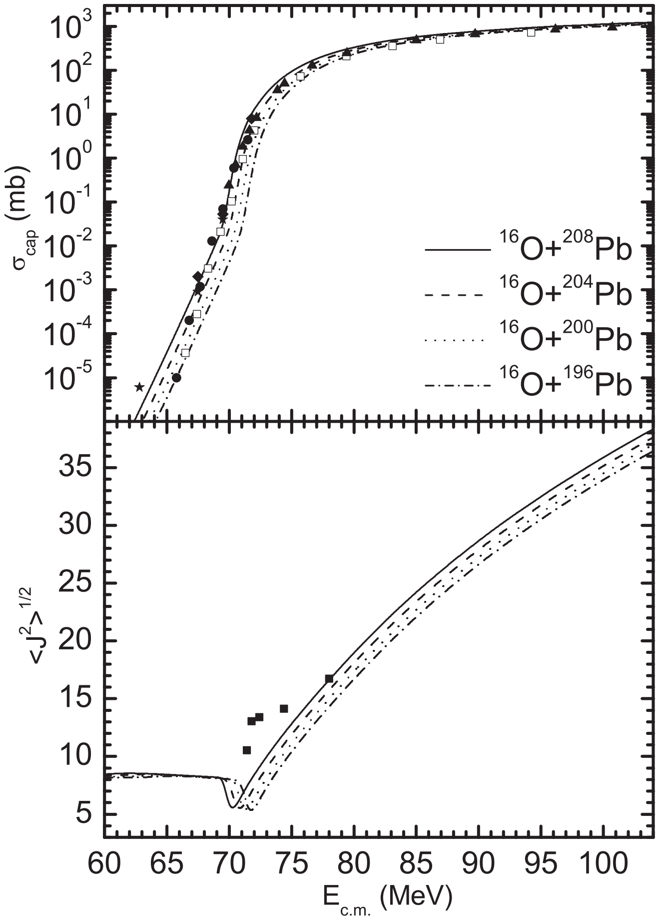

FIG. 9. The calculated capture cross sections (upper part) and the mean-square angular momenta of the captured system (lower part) vs $E_{\rm c.m.}$ for the reactions ^{16}O + ^{196,200,204,208}Pb are compared with the experimental data. The experimental cross sections for the ^{16}O + ^{204}Pb reaction are taken from Ref. [26] (open squares) and for the ^{16}O + ^{208}Pb from Refs. [27] (closed triangles), [28] (closed rhombuses), [26] (closed circles), and [29] (closed stars). The experimental values of $\langle J^2\rangle$ (closed squares) for the ^{16}O + ^{208}Pb reaction are from Ref. [30]. The heights V_b of the Coulomb barriers are 74.6 MeV, 74.2 MeV, 73.6 MeV, and 73.0 MeV, respectively.

$$P_{\rm cap} = \lim_{t\to\infty}\int_{-\infty}^{r_{\rm in}} dR \int_{-\infty}^{\infty} dP\; G(R,P,t|R_0,P_0,0) = \lim_{t\to\infty}\frac{1}{2}\,{\rm erfc}\left[\frac{-r_{\rm in}+\overline{R(t)}}{\sqrt{\Sigma_{RR}(t)}}\right]. \quad (9)$$

The second line in Eq. (9) is obtained by using the propagator $G = \pi^{-1}|\det\Sigma^{-1}|^{1/2}\exp(-\mathbf{q}^T\Sigma^{-1}\mathbf{q})$ [$\mathbf{q}^T = (q_R, q_P)$, $q_R(t) = R - \overline{R(t)}$, $q_P(t) = P - \overline{P(t)}$, $R_0 = \overline{R(t=0)}$, $P_0 = \overline{P(t=0)}$, $\Sigma_{kk'}(t) = 2\overline{q_k(t)q_{k'}(t)}$, $\Sigma_{kk'}(t=0) = 0$, $k,k' = R,P$] calculated for an inverted oscillator which approximates the nucleus-nucleus potential V in the variable R. The frequency ω of this oscillator with an internal turning point $r_{\rm in}$ (Fig. 3) is defined from the condition of equality of the classical actions of approximated and realistic potential barriers of the same height at a given J. It should be noted that the passage through the Coulomb barrier approximated by a parabola has been previously studied in Refs. [11,16]. This approximation is well justified for the reactions and energy range, which are considered here. Finally, one can find the expression for the capture probability:

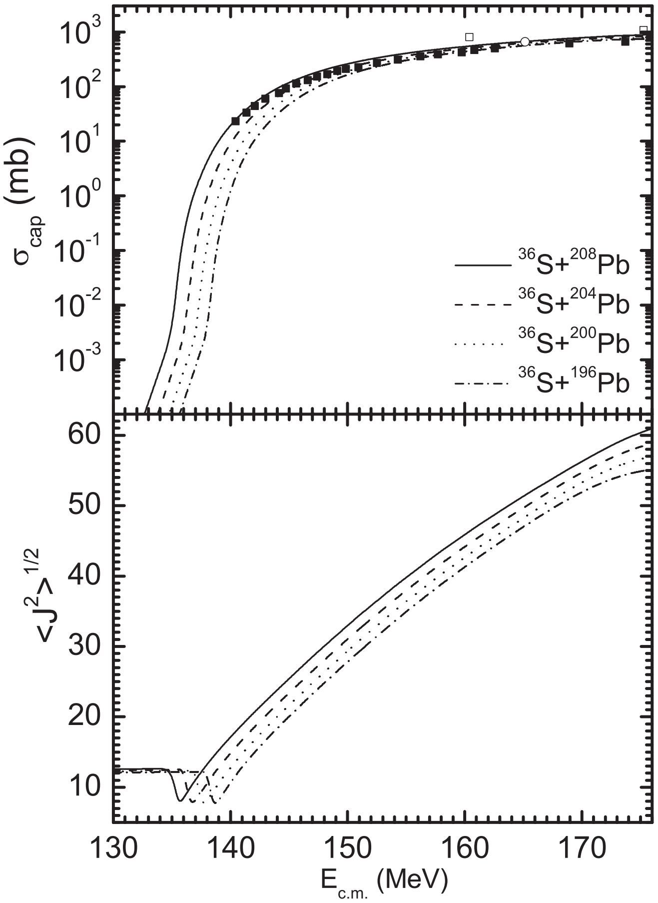

FIG. 10. The same as in Fig. 9, but for the reactions ^{36}S + ^{196,200,204,208}Pb. The experimental cross sections for the ^{36}S + ^{208}Pb reaction are taken from Refs. [31] (closed squares) and [32] (open circles and squares). The heights V_b of the Coulomb barriers are 142.7 MeV, 141.9 MeV, 140.9 MeV, and 139.8 MeV, respectively.

$$P_{\rm cap} = \frac{1}{2}{\rm erfc}\left[\left(\frac{\pi s_1(\gamma - s_1)}{2\mu\hbar\left(\omega_0^2 - s_1^2\right)}\right)^{1/2} \frac{\mu\omega_0^2 R_0/s_1 + P_0}{[\gamma\ln(\gamma/s_1)]^{1/2}}\right], \quad (10)$$

where γ is the internal-excitation width, $\omega_0^2 = \omega^2\{1 - \hbar\tilde{\lambda}\gamma/[\mu(s_1+\gamma)(s_1+\gamma)]\}$ is the renormalized frequency in the Markovian limit, and the value of $\tilde{\lambda}$ is related to the strength of linear coupling in coordinates between collective and internal subsystems. The s_i are the real roots ($s_1 \geqslant 0 > s_2 \geqslant s_3$) of the following equation: $(s+\gamma)(s^2-\omega_0^2) + \hbar\tilde{\lambda}\gamma s/\mu = 0$. The details of the used formalism are presented in Ref. [9]. We have to mention that most of the quantum mechanical effects, dissipative effects, and non-Markovian effects accompanying the passage through the potential barrier are taken into consideration in our formalism [9–11]. For example, the non-Markovian effects appear in the calculations through the internal-excitation width γ.

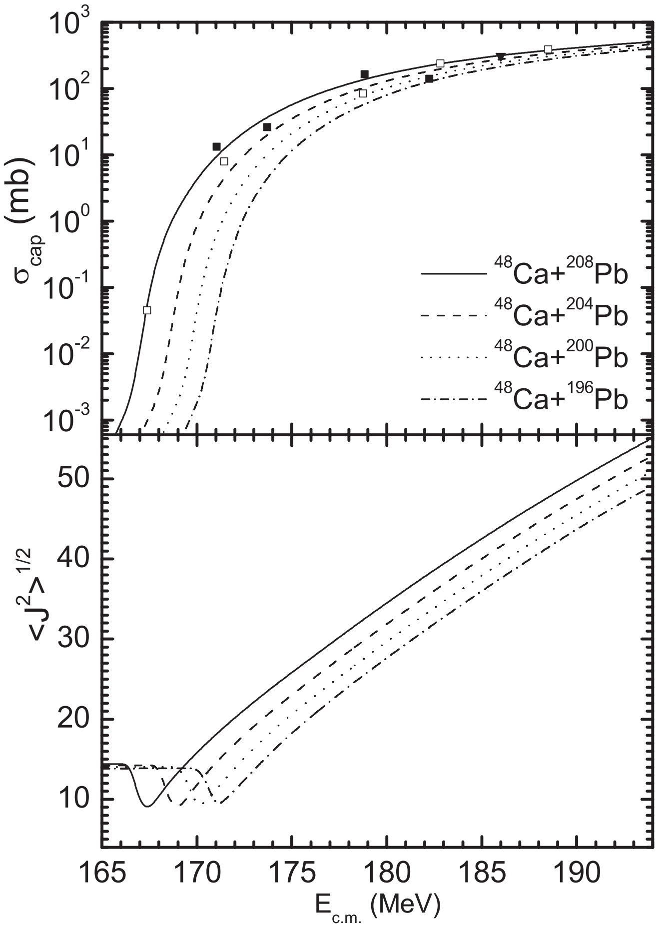

FIG. 11. The same as in Fig. 9, but for the reactions ^{48}Ca + ^{196,200,204,208}Pb. The experimental cross sections for the ^{48}Ca + ^{208}Pb reaction are taken from Refs. [33] (open squares), [34] (closed triangle), and [35] (closed squares). The heights V_b of the Coulomb barriers are 175.1 MeV, 174.0 MeV, 172.9 MeV, and 171.6 MeV, respectively.

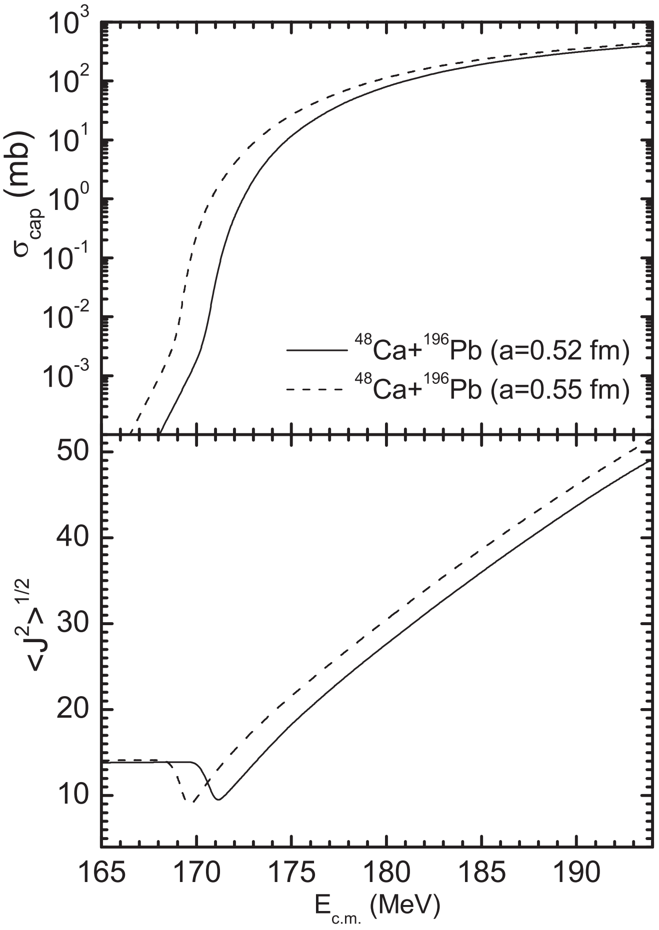

FIG. 12. The capture cross sections (upper part) and the mean-square angular momenta of captured system (lower part) vs $E_{\text{c.m.}}$ for the ^{48}Ca + ^{196}Pb reaction calculated with $a = 0.52$ fm (solid line) and $a = 0.55$ fm (dashed line). The heights V_b of the Coulomb barriers are 175.1 MeV and 173.6 MeV, respectively.

As shown in Fig. 3, the nuclear forces start to play a role at $R_{\text{int}} \approx R_b + 1.1$ fm, where the nucleon density of colliding nuclei approximately reaches 10% of the saturation density. If the value of r_{ex} corresponding to the external turning point is larger than the interaction radius R_{int}, we take $R_0 = r_{\text{ex}}$ and $P_0 = 0$ in Eq. (10). For $r_{\text{ex}} < R_{\text{int}}$, it is natural to start our treatment with $R_0 = R_{\text{int}}$ and P_0 defined by the kinetic energy at $R = R_0$. In this case the friction hinders the classical motion to proceed toward smaller values of R. If $P_0 = 0$ at $R_0 > R_{\text{int}}$, the friction almost does not play a role in the transition through the barrier. So, at $R < R_{\text{int}}$ the relative motion may be more coupled with other degrees of freedom. At $R > R_{\text{int}}$ the relative motion is almost independent of the internal degrees of freedom. Thus, two regimes of interaction at sub-barrier energies differ by the action of the nuclear forces and the role of friction at $R = r_{\text{ex}}$.

III. CALCULATED RESULTS

Besides the parameters related to the nucleus-nucleus potential, two parameter $\hbar\gamma = 15$ MeV and the friction coefficient $\hbar\lambda = -\hbar(s_1 + s_2) = 2$ MeV are used for calculating the capture probability in all reactions. The most realistic friction coefficients in the range of $\hbar\lambda \approx 1$–2 MeV are suggested from the study of deep inelastic and fusion reactions [24]. These values are close to those calculated within the mean field approach [25]. All calculated results presented are obtained with the same set of parameters and are rather insensitive to reasonable variations of them [9,10].

A. Nucleus-nucleus potentials

In Figs. 4 and 5 the nucleus-nucleus potentials calculated for the reactions ^{4}He, ^{16}O, ^{36}S, ^{48}Ca + ^{196,200,204,208}Pb at zero angular momentum are shown. The height of the Coulomb barrier grows with decreasing neutron number of Pb (Fig. 6). For example, V_b changes from 171.5 MeV (19.30 MeV) to 175 MeV (19.75 MeV) for the ^{48}Ca + ^{A}Pb (^{4}He + ^{A}Pb) system when A decreases from 208 to 196. So, the more asymmetric reaction results in the smaller change of the nucleus-nucleus potential.

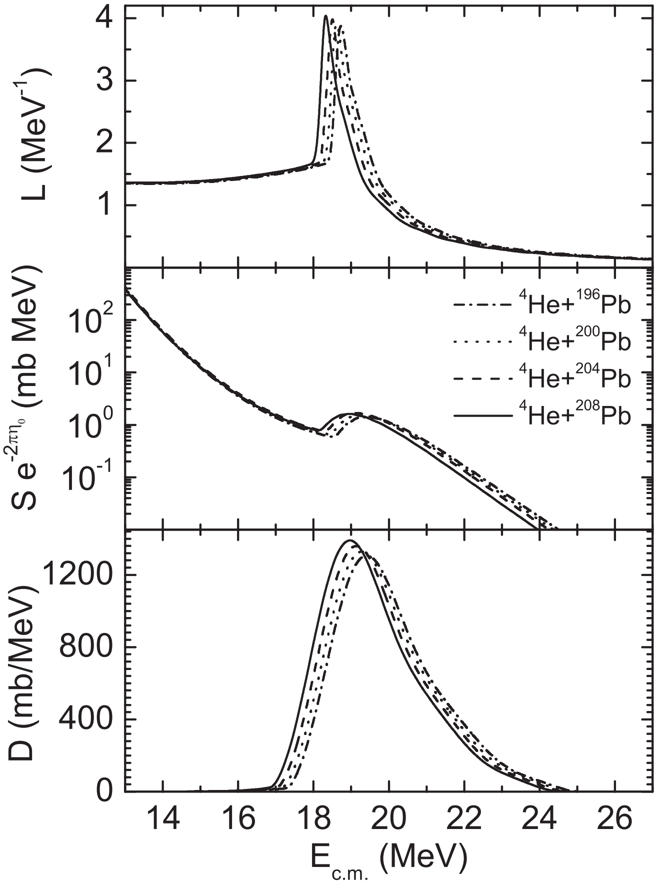

FIG. 13. The calculated values of the astrophysical S factor with $\eta_0 = \eta$ ($E_{\rm c.m.} = V_b$) (middle part), the logarithmic derivative L (upper part), and the fusion barrier distribution $D = d^2(E_{\rm c.m.}\sigma_{cap})/dE^2_{\rm c.m.}$ (lower part) versus $E_{\rm c.m.}$ for the reactions ^{4}He + ^{196}Pb (dash-dotted lines), ^{200}Pb (dotted lines), ^{204}Pb (dashed lines), and ^{208}Pb(solid lines).

With decreasing mass number of Pb isotope the pocket depth B_{qf} becomes smaller (Fig. 7) as well as the distance between the positions of the pocket minimum and the Coulomb barrier at $R = R_b \approx R_1 + R_2 + 2$ fm, where $R_i = 1.15A_i^{1/3}$ ($i = 1, 2$) are the radii of colliding nuclei (Fig. 7). For example, $B_{qf} = 3.2$ MeV (15 MeV) and 4.8 MeV (16.4 MeV) for the reactions ^{48}Ca + ^{196}Pb (^{4}He + ^{196}Pb) and ^{48}Ca + ^{208}Pb (^{4}He + ^{208}Pb), respectively. As seen in Fig. 7, the value of $\omega_b = |\partial^2 V/\partial R^2|_{R=R_b}$ is almost insensitive to the neutron number of the dinuclear system.

As the centrifugal part of the potential grows, the potential pocket becomes shallower, while the position of the pocket minimum moves toward the barrier at $R = R_b$. At some critical angular momentum the potential pocket disappears and the value of capture cross section goes to zero.

B. Capture cross section and mean-square angular momentum of captured system

In Figs. 8–11 the calculated capture cross sections for the reactions ^{4}He,^{16}O,^{36}S,^{48}Ca + ^{196,200,204,208}Pb are presented. The calculated results are in rather good agreement with the available experimental data. As is seen, the decrease of the Pb atomic number leads to smaller values of capture cross section at fixed $E_{\rm c.m.}$ for all types of the reactions. So, as the Pb diffuseness parameter becomes smaller, the height of the Coulomb barrier becomes larger and, accordingly, the capture cross section becomes smaller at a certain value of $E_{\rm c.m.}$. Thus, the increase of the number of neutrons in Pb assists the capture process. In Fig. 9 the experimental data are for the reactions ^{16}O + ^{204,208}Pb. They demonstrate the same behavior like the calculated solid and dashed curves. The isotopic dependence is rather weak because the nucleus-nucleus potential weakly depends on the mass number of the target in very asymmetric reactions. In the reactions with ^{48}Ca the isotopic trend is more pronounced.

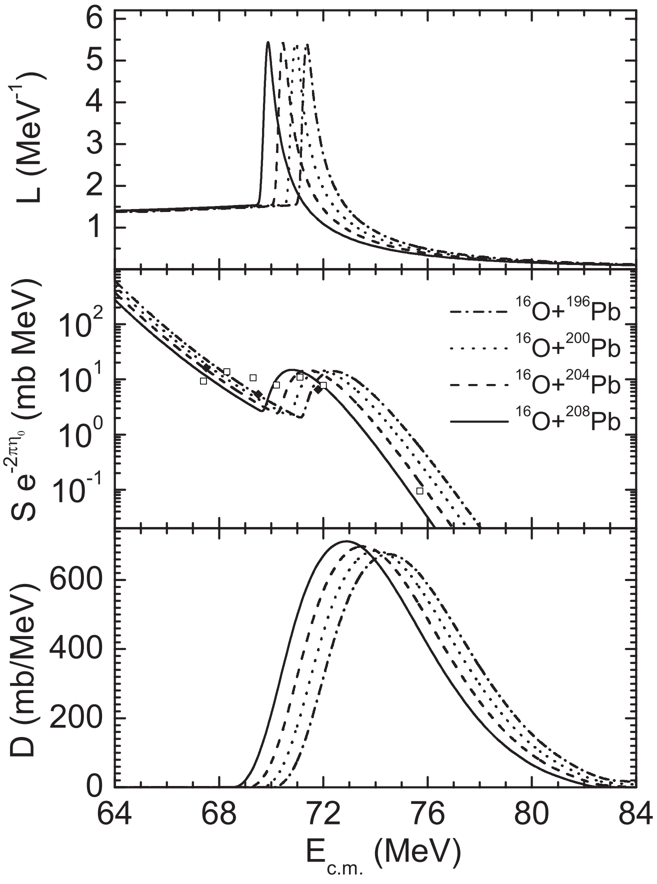

FIG. 14. The same as in Fig. 13, but for the reactions ^{16}O + ^{196,200,204,208}Pb. The experimental data for the reactions ^{16}O + ^{204}Pb and ^{16}O + ^{208}Pb are taken from Ref. [26] (open squares) and Ref. [28] (closed rhombuses), respectively.

In Figs. 8–11 one can see that there is a sharp dropoff of the cross sections just under the Coulomb barrier. With decreasing $E_{\rm c.m.}$ up to about 0.5–5.0 MeV below the Coulomb barrier, the regime of interaction is changed because at the external turning point the colliding nuclei do not reach the region of nuclear interaction where friction plays a role. As a result, at smaller $E_{\rm c.m.}$ the cross sections fall with a smaller rate. With large values of $R_{\rm int}$ the change of fall rate occurs at smaller $E_{\rm c.m.}$. However, the uncertainty in the definition of $R_{\rm int}$ is rather small. This effect is not sensitive to the change of mass number of Pb. Therefore, the change of fall rate of

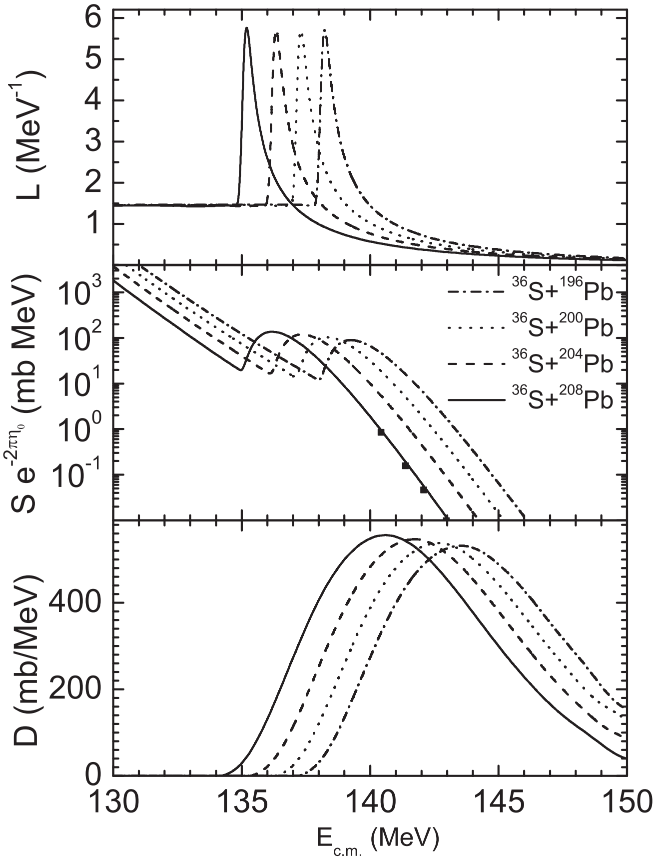

FIG. 15. The same as in Fig. 13, but for the reactions ^{36}S + ^{196,200,204,208}Pb. The experimental data for the ^{36}S + ^{208}Pb reaction are taken from Ref. [31] (closed squares).

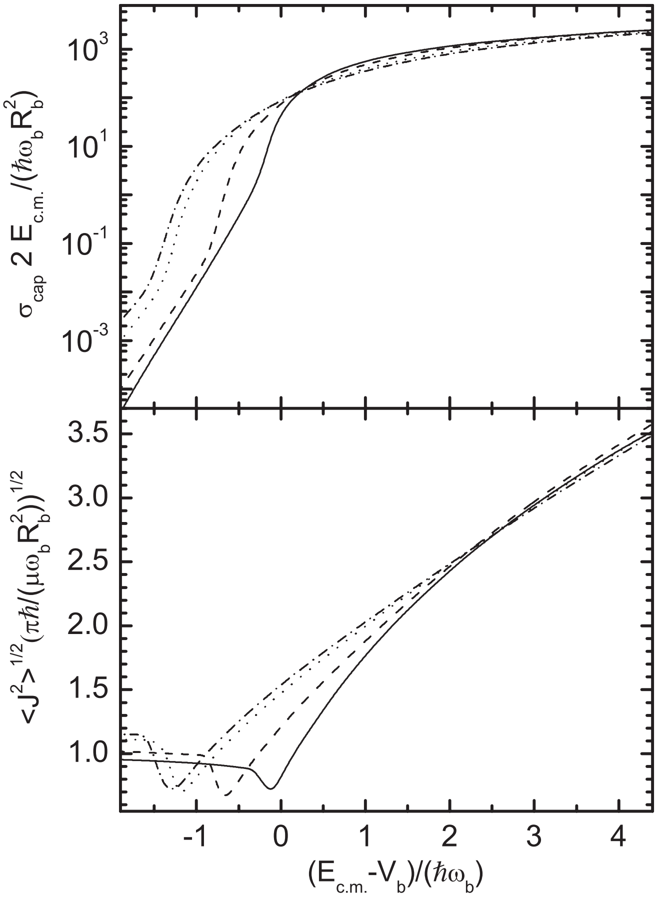

FIG. 16. The calculated reduced capture cross sections (upper part) and the mean-square angular momenta of the captured system (lower part) vs $(E_{\rm c.m.} - V_b)/(\hbar\omega_b)$. Solid, dashed, dotted, and dash-dotted lines show the results for the reactions ^{4}He + ^{A}Pb, ^{16}O + ^{A}Pb, ^{36}S + ^{A}Pb, and ^{48}Ca + ^{A}Pb, respectively.

sub-barrier capture cross section should be in the data if we assume that the friction starts to act only when the colliding nuclei approach the barrier. Note that experimental data have still large uncertainties to make a firm experimental conclusion about this effect.

The calculated mean-square angular momenta of captured systems vs $E_{\rm c.m.}$ are presented in Figs. 8–11 as well. The increase of A raises the mean-square angular momentum of captured system, as expected. At energies 0.5–4.5 MeV below the barrier $\langle J^2\rangle$ has a minimum. The position of the minimum is shifted to the smaller energies with increasing A. Note that there are experimental indications [30] of the presence of this minimum. On the left-hand side of this minimum the dependence of $\langle J^2\rangle$ on $E_{\rm c.m.}$ is rather weak. A similar weak dependence has been found in Ref. [36] in the extreme sub-barrier region. Note that the found behavior of $\langle J^2\rangle$, which is related to the change of the regime of interaction between the colliding nuclei, would affect the angular anisotropy of the products of fission-like fragments following capture. Indeed, the values of $\langle J^2\rangle$ are extracted from data on angular distribution of fission-like fragments [4].

In Fig. 12 the calculated capture cross sections and the mean-square angular momenta of captured system are presented versus $E_{\rm c.m.}$ for the ^{48}Ca + ^{196}Pb reaction with diffuseness parameter $a = 0.52$ fm (as in Fig. 11) and $a = 0.55$ fm for ^{196}Pb. The change of a causes the change of the Coulomb barrier, which leads to increase or decrease of the capture cross section. So, the choice of the diffuseness parameter significantly affects the value of capture cross section especially in the sub-barrier region. If we use $a = 0.55$ fm for all Pb isotopes then all capture cross section and mean-square angular momentum dependencies will be closer to each other than in Figs. 8–11.

C. Astrophysical *S* factor, *L* factor, and barrier distribution

Assuming that the capture cross section is equal to the fusion cross section, we calculate astrophysical S factor, $S = E_{\rm c.m.}\sigma_{\rm cap}\exp(2\pi\eta)$. Here, $\eta(E_{\rm c.m.}) = Z_1Z_2e^2\sqrt{\mu/(2\hbar^2E_{\rm c.m.})}$ is the Sommerfeld parameter. In Figs. 13–15 the calculated S factors versus $E_{\rm c.m.}$ are shown for the reactions ^{4}He, ^{16}O, ^{36}S + ^{A}Pb. The S factor has a maximum. In Figs. 14 and 15 the behavior of the S factor in the reactions ^{16}O + ^{204,208}Pb and ^{36}S + ^{208}Pb is well reproduced. After this maximum the S factor slightly decreases with decreasing $E_{\rm c.m.}$ and then starts to increase. The same behavior has been revealed in Ref. [37] by extracting the S factor from the experimental data for lighter systems. In Figs. 13–15, the so-called logarithmic

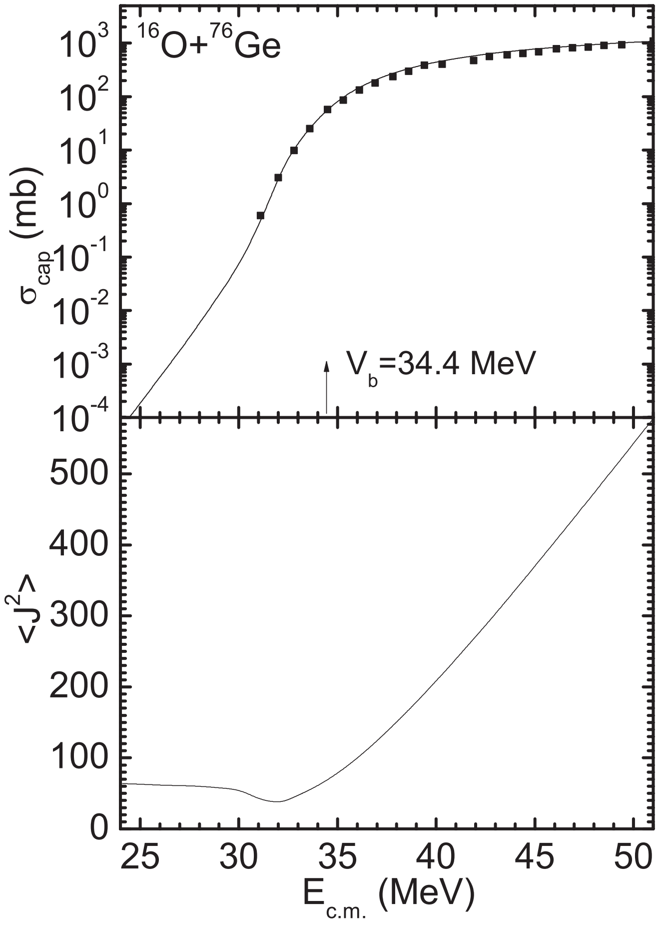

FIG. 17. The calculated capture cross sections (upper part) and mean-square angular momenta of the captured system (lower part) vs $E_{\mathrm{c.m.}}$ for the $^{16}\mathrm{O} + {}^{76}\mathrm{Ge}$ reaction. The experimental cross sections are from Ref. [39] (closed squares). The height V_b of the Coulomb barrier is indicated by the arrow. The quadrupole deformation parameters are $\beta_1(^{16}\mathrm{O}) = 0$ and $\beta_2(^{76}\mathrm{Ge}) = 0.2623$ [22].

derivative, $L(E_{\mathrm{c.m.}}) = d[\ln(E_{\mathrm{c.m.}}\sigma_{\mathrm{cap}})]/dE_{\mathrm{c.m.}}$, and the barrier distribution $d^2(E_{\mathrm{c.m.}}\sigma_{\mathrm{cap}})/dE^2_{\mathrm{c.m.}}$ are also presented for the reactions ^{4}He, ^{16}O, ^{36}S + ^{A}Pb. The logarithmic derivative strongly increases below the barrier and then has a maximum at $E_{\mathrm{c.m.}} \approx V_b - 3$ MeV. The maximum of L almost corresponds to the minimum of the S factor. The barrier distributions calculated have only one maximum at $E_{\mathrm{c.m.}} = V_b$. For the S factor and L and D functions, the value of height of maximum increases slightly with A. The widths of these maxima are almost independent of the mass number of Pb. The positions of maxima are shifted to larger $E_{\mathrm{c.m.}}$ with decreasing A. The position of the maximum of the D function corresponds to the Coulomb barrier. As seen in Figs. 13–15, the positions of the maxima of S and D come closer to each other with increasing reaction asymmetry. The maximum of the S factor is expected at σ_{cap} of about 10 mb in the reactions with ^{4}He and at σ_{cap} of about 0.1 mb in the reactions with ^{36}S. Therefore, the observation of the maximum and minimum of S is simpler in the strongly asymmetric reactions.

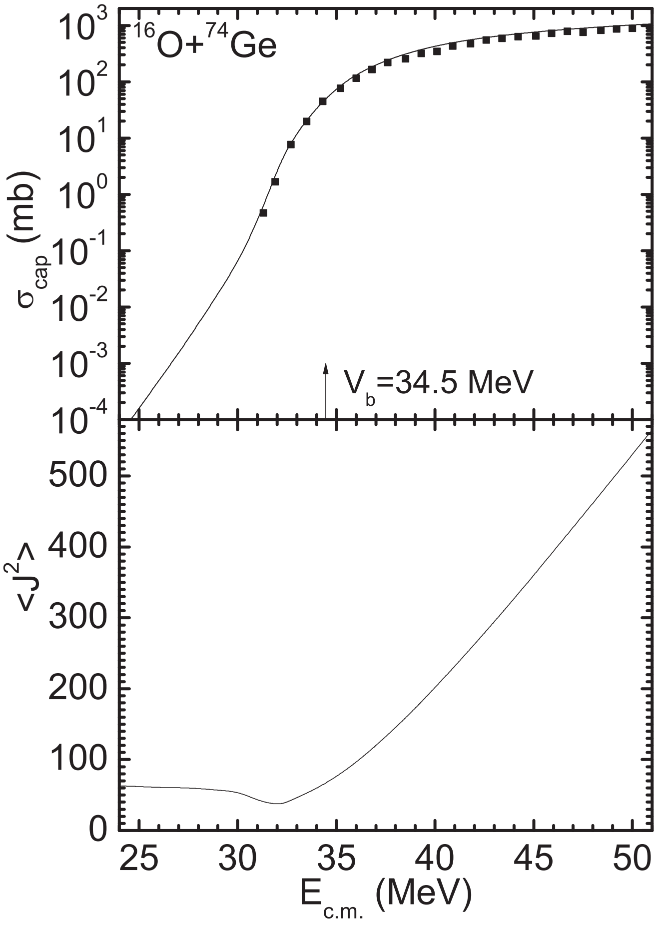

FIG. 18. The same as in Fig. 17, but for the $^{16}\mathrm{O} + {}^{74}\mathrm{Ge}$ reaction. The experimental cross sections are from Ref. [39] (closed squares). The static quadrupole deformation parameters are $\beta_1(^{16}\mathrm{O}) = 0$ and $\beta_2(^{74}\mathrm{Ge}) = 0.2825$ [22].

D. Dimensionless representations of capture cross sections and mean-square angular momenta

In Ref. [38] a reduction procedure was proposed to eliminate the influence of the nucleus-nucleus potential (the Coulomb barrier height, width, and position) on the fusion (capture) cross section. It consists of the following transformations:

$$E_{\mathrm{c.m.}} \to \frac{E_{\mathrm{c.m.}} - V_b}{\hbar\omega_b}, \quad \sigma_{\mathrm{cap}} \to \frac{2E_{\mathrm{c.m.}}}{\hbar\omega_b R_b^2}\sigma_{\mathrm{cap}},$$
$$\langle J^2\rangle^{1/2} \to \left[\frac{\pi\hbar}{\mu\omega_b R_b^2}\right]^{1/2}\langle J^2\rangle^{1/2}. \tag{11}$$

To unify the obtained results for all reactions with ^{A}Pb isotopes, we present in Fig. 16 the calculated capture cross sections and the mean-square angular momenta of captured systems in the dimensionless representation [38]. As it is seen from the Fig. 16, the reduced values of cross section and mean-square angular momentum of captured systems in the reactions $^4\mathrm{He} + {}^{196,200,204,208}\mathrm{Pb}$ coincide at bombarding energies above and below the Coulomb barrier. The same behavior can be observed for other groups of the reactions $^{16}\mathrm{O} + {}^{196,200,204,208}\mathrm{Pb}$,

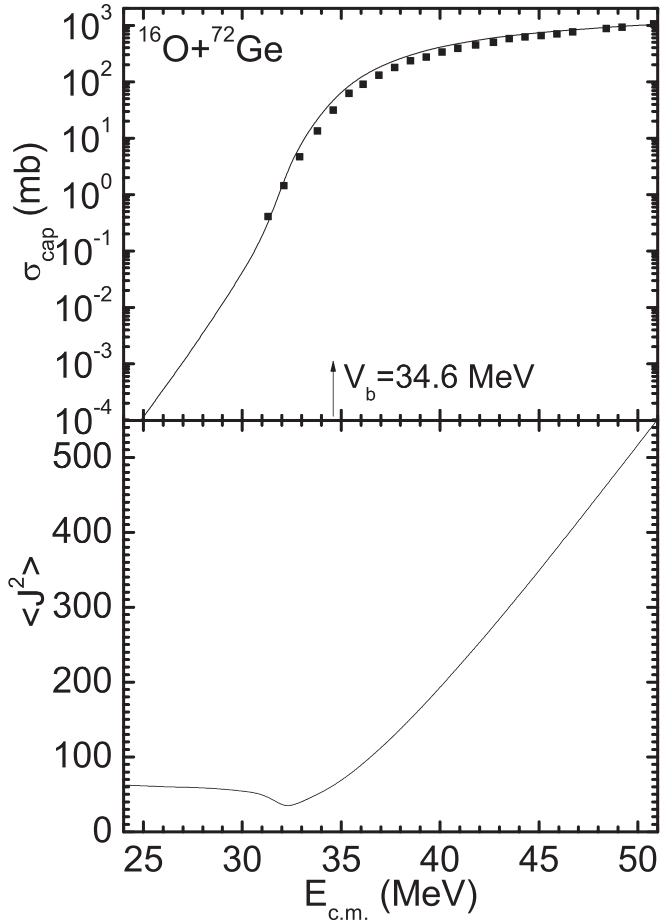

FIG. 19. The same as in Fig. 17, but for the ^{16}O + ^{72}Ge reaction. The experimental cross sections are from Ref. [39] (closed squares). The quadrupole deformation parameters are $\beta_1(^{16}\text{O}) = 0$ and $\beta_2(^{72}\text{Ge}) = 0.2424$ [22].

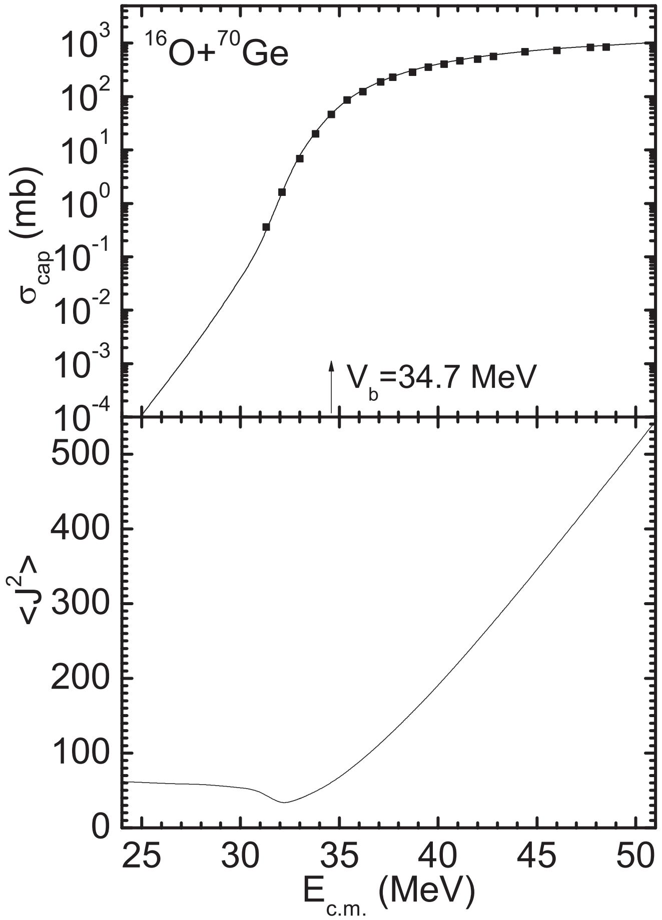

FIG. 20. The same as in Fig. 17, but for the ^{16}O + ^{70}Ge reaction. The experimental cross sections are from Ref. [39] (closed squares). The quadrupole deformation parameters are $\beta_1(^{16}\text{O}) = 0$ and $\beta_2(^{70}\text{Ge}) = 0.2245$ [22].

^{36}S + ^{196,200,204,208}Pb, and ^{48}Ca + ^{196,200,204,208}Pb. From this behavior and from the very weak dependencies of ω_b and R_b on the neutron number of the dinuclear system (see Fig. 7), one can conclude that the neutron number or the diffuseness parameter strictly influences the capture cross section through only the height of the Coulomb barrier. So, by using the nucleus-nucleus interaction potential calculated with any realistic diffuseness parameter and adjusting the height of the Coulomb barrier from experimental capture cross sections at bombarding energies near the barrier, one can calculate the capture cross sections or any other observables at sub-barrier energies. Such types of calculations are suitable to describe the capture of deformed nuclei for which the self-consistent calculations of diffusenesses are not available. In addition, the diffuseness seems to be dependent on the angle with respect to the symmetry axis of the deformed nucleus.

As found, the change of the neutron number in one of the colliding nuclei mainly causes the change of the height of the Coulomb barrier. If this height is adjusted to the experimental data, the nucleus-nucleus potential can be calculated at some fixed realistic values of parameters irrespective of the number of neutrons in the system. For the reactions ^{16}O + ^{70,72,74,76}Ge with deformed target nuclei, the heights of the calculated Coulomb barriers $V_b = V(R_b)$ are adjusted to the experimental data [39] for the capture cross section at $E_{\text{c.m.}} \geqslant V_b$. We use $r_0 = 1.15$ fm and $a = 0.55$ fm for all deformed nuclei ^{70,72,74,76}Ge. The experimental quadrupole deformation parameters of the isotopes ^{70,72,74,76}Ge are taken from Ref. [22]. In these reactions there are no neutron transfer channels with positive Q values and thus transfer might be expected to be suppressed. In Figs. 17–20, the calculated capture cross sections for the reactions ^{16}O + ^{70,72,74,76}Ge are in a rather good agreement with the available experimental data. One can see that there is a sharp dropoff of the cross sections just under the Coulomb barrier. At $E_{\text{c.m.}}$ of 3.5–4.0 MeV below the Coulomb barrier the regime of interaction is changed (turning off the nuclear forces and, respectively, nuclear friction). As a result, at smaller $E_{\text{c.m.}}$ the cross sections fall with a smaller rate, but the effect is less pronounced in contrast to the collisions of spherical nuclei. The collisions of deformed nuclei occur at various mutual orientations affecting the value of R_{int}.

In Figs. 17–20, the calculated mean-square angular momenta of the captured systems versus $E_{\text{c.m.}}$ are predicted for the reactions ^{16}O + ^{70,72,74,76}Ge.

IV. SUMMARY

By using the quantum diffusion approach, we studied the isotopic trends of capture cross sections and mean-square angular momenta of captured systems in the reactions ^{4}He, ^{16}O, ^{36}S, ^{48}Ca + ^{196,200,204,208}Pb. The nuclear parts of the nucleus-nucleus interaction potentials were calculated by using the double-folding procedure with the density-dependent effective NN interaction [18] constructing with an averaging procedure from the TFFS effective interaction. For density distributions of interacting nuclei, we used the two-parameter symmetrized Fermi functions. For the lead isotopes, the Fermi-distribution parameters were found to fit to the self-consistent density distributions calculated with the DF3-a functional [21] within the EDF method [20].

The available experimental data at energies above and below the Coulomb barrier are well described. The isotopic trends are attributed to the deformation effects, neutron transfer, and nucleus-nucleus interaction. As demonstrated in our calculations, in the case of the same deformations of colliding isotopes and minor effect of neutron transfer, the neutron number of the target nucleus strictly influences the height of the Coulomb barrier but not the width of the barrier. Thus, the height V_b of the calculated Coulomb barrier can be adjusted to the experimental data for the capture cross sections at $E_{\text{c.m.}} \geqslant V_b$ to take effectively into account the change of nuclear interaction with neutron number. The width of the nucleus-nucleus interaction potential can be calculated with any realistic diffuseness parameter because the width is rather insensitive to its value. Indeed, this procedure is often used for calculating the sub-barrier fusion and capture. It was applied to the reactions ^{16}O + ^{70,72,74,76}Ge.

As found, the increase of the number of neutrons in Pb assists the capture process. The isotopic dependence is rather weak in the reactions ^{4}He, ^{16}O + ^{196,200,204,208}Pb because the nucleus-nucleus potential weakly depends on the mass number of the target in very asymmetric reactions. In the reactions with ^{36}S and ^{48}Ca the isotopic trend is more pronounced. The slope of the capture cross section at deep sub-barrier energies is not sensitive to the neutron number of the system.

ACKNOWLEDGMENTS

The work was partly supported by Grants No. NSh-7235.2010.2 and No. 2.1.1/4540 of the Russian Ministry for Science and Education, by the RFBR Grants No. 11-02-00467-a and No. 10-02-00301-a, and the DFG.

[1] C. A. Bertulani, EPJ Web Conf. **17**, 15001 (2011).
[2] Z. Kohley *et al.*, Phys. Rev. Lett. **107**, 202701 (2011).
[3] F. Scarlassara *et al.*, EPJ Web Conf. **17**, 05002 (2011).
[4] H. Q. Zhang *et al.*, Phys. Rev. C **81**, 034611 (2010).
[5] G. Montagnoli *et al.*, Phys. Rev. C **82**, 064609 (2010).
[6] M. G. Itkis *et al.*, Nucl. Phys. A **834**, 374C (2010).
[7] G. Hupin and D. Lacroix, Phys. Rev. C **81**, 014609 (2010); S. Ayik, B. Yilmaz, and D. Lacroix, *ibid.* **81**, 034605 (2010).
[8] V. Yu. Denisov and N. A. Pilipenko, Phys. Rev. C **81**, 025805 (2010).
[9] V. V. Sargsyan, G. G. Adamian, N. V. Antonenko, and W. Scheid, Eur. Phys. J. A **45**, 125 (2010); V. V. Sargsyan, G. G. Adamian, N. V. Antonenko, W. Scheid, and H. Q. Zhang, *ibid.* **47**, 38 (2011); Phys. Rev. C **84**, 064614 (2011); **85**, 024616 (2012).
[10] V. V. Sargsyan, G. G. Adamian, N. V. Antonenko, W. Scheid, and H. Q. Zhang, J. Phys.: Conf. Ser. **282**, 012001 (2011); EPJ Web Conf. **17**, 04003 (2011).
[11] V. V. Sargsyan, Z. Kanokov, G. G. Adamian, N. V. Antonenko, and W. Scheid, Phys. Rev. C **80**, 034606 (2009); **80**, 047603 (2009); V. V. Sargsyan, Z. Kanokov, G. G. Adamian, and N. V. Antonenko, Part. Nucl. **41**, 175 (2010).
[12] K. Langanke and C. A. Barnes, Adv. Nucl. Phys. **22**, 173 (1996).
[13] A. Aprahamian, K. Langanke, and M. Wiescher, Prog. Part. Nucl. Phys. **54**, 535 (2005).
[14] A. S. Zubov, V. V. Sargsyan, G. G. Adamian, and N. V. Antonenko, Phys. Rev. C **84**, 044320 (2011).
[15] A. S. Zubov, V. V. Sargsyan, G. G. Adamian, N. V. Antonenko, and W. Scheid, Phys. Rev. C **81**, 024607 (2010); **82**, 034610 (2010).
[16] H. Hofmann, Phys. Rep. **284**, 137 (1997); C. Rummel and H. Hofmann, Nucl. Phys. A **727**, 24 (2003).
[17] N. Takigawa, S. Ayik, K. Washiyama, and S. Kimura, Phys. Rev. C **69**, 054605 (2004); S. Ayik, B. Yilmaz, A. Gokalp, O. Yilmaz, and N. Takigawa, *ibid.* **71**, 054611 (2005).
[18] G. G. Adamian *et al.*, Int. J. Mod. Phys. E **5**, 191 (1996).
[19] A. B. Migdal, *Theory of Finite Fermi Systems and Applications to Atomic Nuclei* (Wiley, New York, 1967).
[20] S. A. Fayans, S. V. Tolokonnikov, E. L. Trykov, and D. Zawischa, Nucl. Phys. A **676**, 49 (2000).
[21] S. V. Tolokonnikov and E. E. Saperstein, Phys. Atom. Nucl. **73**, 1684 (2010).
[22] S. Raman, C. W. Nestor, and P. Tikkanen, At. Data Nucl. Data Tables **78**, 1 (2001).
[23] E. E. Saperstein and S. V. Tolokonnikov, Phys. Atom. Nucl. **73**, 1277 (2011).
[24] G. G. Adamian, A. K. Nasirov, N. V. Antonenko, and R. V. Jolos, Phys. Part. Nucl. **25**, 587 (1994).
[25] K. Washiyama, D. Lacroix, and S. Ayik, Phys. Rev. C **79**, 024609 (2009); S. Ayik, K. Washiyama, and D. Lacroix, *ibid.* **79**, 054606 (2009).
[26] M. Dasgupta, D. J. Hinde, A. Diaz-Torres, B. Bouriquet, C. I. Low, G. J. Milburn, and J. O. Newton, Phys. Rev. Lett. **99**, 192701 (2007).
[27] C. R. Morton, A. C. Berriman, M. Dasgupta, D. J. Hinde, J. O. Newton, K. Hagino, and I. J. Thompson, Phys. Rev. C **60**, 044608 (1999).
[28] S. P. Tretyakova *et al.*, Nucl. Phys. A **734**, E33 (2004); **738**, 487 (2004).
[29] Yu. Ts. Oganessian *et al.*, JINR Rapid Commun. **75**, 123 (1996).
[30] R. Vandenbosch, Annu. Rev. Nucl. Part. Sci. **42**, 447 (1992).
[31] D. J. Hinde, M. Dasgupta, N. Herrald, R. G. Neilson, J. O. Newton, and M. A. Lane, Phys. Rev. C **75**, 054603 (2007).
[32] W. Loveland *et al.*, Phys. Rev. C **74**, 044607 (2006).
[33] E. Prokhorova *et al.*, Nucl. Phys. A **802**, 45 (2008).
[34] R. Bock *et al.*, Nucl. Phys. A **388**, 334 (1982).

[35] A. J. Pacheco *et al.*, Phys. Rev. C **45**, 2861 (1992).
[36] A. B. Balantekin, J. R. Bennett, and S. Kuyucak, Phys. Lett. B **335**, 295 (1994).
[37] K. Langanke and S. E. Koonin, Nucl. Phys. A **410**, 334 (1983); A. Redder *et al.*, *ibid.* **462**, 385 (1987).
[38] L. F. Canto, P. R. S. Gomes, J. Lubian, L. C. Chamon, and E. Crema, J. Phys. G **36**, 015109 (2009); Nucl. Phys. A **821**, 51 (2009); P. R. S. Gomes *et al.*, *ibid.* **828**, 233 (2009).
[39] E. F. Aguilera, J. J. Kolata, and R. J. Tighe, Phys. Rev. C **52**, 3103 (1995).